Construction and Building Materials 165 (2018) 218–231

Contents lists available at ScienceDirect

Construction and Building Materials

journal homepage: www.elsevier.com/locate/conbuildmat

3D printing of reinforced concrete elements: Technology and design approach

Domenico Asprone [a], Ferdinando Auricchio [b], Costantino Menna [a,*], Valentina Mercuri [b]

[a] Department of Structures for Engineering and Architecture, University of Naples Federico II, Italy
[b] Department of Civil Engineering and Architecture, University of Pavia, Italy

HIGHLIGHTS

- We present the fabrication of RC members based on concrete 3D printing technology.
- A straight 3.00 m long RC beam is manufactured and tested under 3-point bending.
- A second RC beam has been also 3D printed with variable cross section.
- The approach will facilitate the production of free-form structurally optimized RC structures.

ARTICLE INFO

Article history:
Received 1 October 2017
Received in revised form 19 December 2017
Accepted 3 January 2018

Keywords:
Additive manufacturing
Concrete
Digital fabrication
Reinforced concrete
Flexural behavior

ABSTRACT

This paper deals with a novel approach to the fabrication of reinforced concrete (RC) members based on Concrete 3D printing technology. The approach consists in the partition of a RC member into different concrete segments printed separately and, then, assembled into a unique element along with the steel reinforcement system. The approach is expected to facilitate the production of free-form structurally optimized RC elements with the final aim of saving concrete material and, at the same time, fabricating lighter structures. As case study, we report on the material characterization and fabrication steps of a straight 3.00 m long RC beam together with the results of a full-scale three-point bending test performed on it. As a demonstration of the potentialities of this approach, the fabrication of a free-form variable cross-section RC beam is also presented.

1. Introduction

Additive manufacturing (AM) has been defined as "the process of joining materials to make objects from 3D model data, usually layer upon layer, as opposed to subtractive manufacturing methodologies, such as traditional machining" [1]. AM technologies are increasingly having an impact on industrial processes in many fields and numerous applications have been developed so far, ranging from, for example, automotive to medical, security and aerospace sectors [2–4]. Advocates of AM argue that this technology represents a new industrial revolution and is enabling the mass customization of industrial production, where small quantities of customized products can be built affordably [2,5].

Until a few years ago, AM technologies were mostly applied to rapid prototyping (RP), i.e. the fabrication of prototypes used for iterative design, inspection and communication tools. In fact, AM technologies were not considered to be able to process common materials with adequate mechanical and physical properties [6]. However, the emerging *digital fabrication*, defined as the application of digital modelling and technologies to the production of custom material objects, promises to revolutionize the traditional manufacturing schemes. Indeed, nowadays AM technologies are successfully implemented to fabricate objects made of ceramics [7], metals [8], and polymers [9] with adequate mechanical properties.

Recently, AM technologies are attracting a growing interest in construction industry as well, especially in the concrete technology. The interest in exploiting AM technologies in construction industry is mainly the result of the expectation of new freedom in terms of the design of shapes, elements and structures, enabling at the same time new aesthetic and functional features (often referred to as *freeform constructions*). In fact, in the construction industry, single components are in most cases unique in dimension. Standardized/traditional manufacturing processes require pieces to be cut through subtractive technologies (in which the

* Corresponding author.
E-mail address: costantino.menna@unina.it (C. Menna).

https://doi.org/10.1016/j.conbuildmat.2018.01.018
0950-0618/

material is machined away to produce the final object - e.g. natural stone, ceramic pavements) or proper moulds to be created. In the latter case, moulds are utilized in combination with formative technologies (where the fresh material is cast in a mould - e.g. reinforced concrete elements) to achieve the final shape of the object [10]. Accordingly, in both cases, architectural designers are often forced to use multiple identical elements in a project to save materials and reduce costs of labour and/or moulds. By changing the approach in the way that components are produced, AM is expected to revolutionize this paradigm, allowing designers to make each component unique without incurring prohibitive costs.

Other advantages of this automated process are also expected, such as the reduction in construction time and expenses, greater worker safety, better quality and reliability, the saving of materials and, consequently, sustainability [11]. Notably, with regard the latter aspect, a recent study has demonstrated that digital fabrication is able to provide environmental benefits when applied to complex structures, for which additional complexity can be achieved without additional environmental costs.

Recently, the combination of digital fabrication techniques and cementitious materials has led to the development of innovative manufacturing processes for fabricating concrete-like products, objects and/or structures; these include Layered Extrusion (contour crafting [12], concrete printing [13], Freeform Construction), Binder Jetting (D-shape [14]), Slip-forming (smart dynamic casting [15]). The detailed review of the methods of digital fabrication with concrete (often referred to as "*digital concrete*") is reported in [11].

To date, most developments in digital fabrication of concrete-like products have been focused on layered extrusion technology (such as contour crafting, concrete printing), probably because its overall operating procedure is based on the more widespread production scheme of polymeric customized parts. However, its implementation in construction processes requires much larger printers (or, more in general, robotic machines) than those used for metal or plastic objects, due to the dimensions of the final objects to be printed. Generally, the automated machinery used for layered extrusion of concrete includes a digitally controlled moving printing head (or nozzle) which precisely lays down the concrete or mortar material layer-by-layer, enabling the opportunity to create customized structures and/or functional voids into the printed elements [16,17]. This manufacturing technology facilitates the development of on-site constructions in one single stage, reducing in this way transportation of construction equipment, assembly operations, labour costs and the risk of injuries during construction works [18].

The engineering challenges related to layered extrusion technology are manifold. Indeed, to effectively exploit the functional/mechanical properties of 3D printed concrete products, the layered extrusion of concrete elements requires the fresh printed material to have some specific rheological properties [19]:

- Pumpability: the capacity to be worked and moved to the printing head through a pumping system throughout a given time interval.
- Extrudability: the capability to be extruded properly through the printing head with a continuous material flow.
- Buildability: the capacity to both remain stacked in layers after extrusion and sustain the weight of the subsequent layers that are deposited by the printing process.

Therefore, the concrete/mortar rheology must be optimized to achieve a balance between the need for workability and extrudability on the one hand – which would require reduced yield stress – and the need for buildability on the other – which would require an increased yield stress. The printing speed is a critical parameter as well, and can have an impact on the mechanical properties of the printed elements. Printing speed must be set based on the rheology of the printed mortar, the dimensions of the objects and the dimensions of the extrusion head. In fact, the time elapsed between the deposition of two layers must be long enough to let the first layer adequately harden and become capable of sustaining the weight of the second layer, but short enough to guarantee that the first layer is still fresh enough to develop a good bond with the second layer [11,20].

Given all the issues and challenges related to the AM of concrete elements, this technology is still not mature enough to be used in the market. In addition, steel reinforcement integration into 3D printed concrete structures is characterized by lower technological progress. Available examples concern the Mesh Mould approach which consists in digitally fabricating metal wires formworks that act as permanent reinforcement during the concreting process [11] or, alternatively, the use of fibres in printable mortars. An effective approach to manufacture traditional steel reinforced concrete elements (i.e. made of concrete and steel rebar) by implementing one of available AM technologies has not been developed so far. One of the main reasons is the scarce adaptability of traditional steel reinforcing systems (in the form of stiff, straight and thick rebar or rods) to a specific/complex shape (large energies are required to bend the reinforcing steel) during the AM process. Nevertheless, researchers in this field are increasing their attention with regard to the opportunities that AM is able to provide also for steel reinforcement embedment.

This paper aims to contribute to this promising line of research, and reports on outcomes of a research program aimed to develop a novel approach to the design and fabrication of reinforced concrete (RC) beam elements, based on AM technology.

In the following sections, the scope and basic idea of the fabrication approach are firstly introduced. Accordingly, the design framework is defined, and then the experimental and numerical outcomes of the first full-scale 3D printed RC beam are discussed along with the expected advantages and critical issues arose.

2. Material and methods

2.1. A novel approach to the manufacturing of RC elements

The main objective of the fabrication approach herein presented consists in manufacturing steel RC beams using AM technology of concrete. The implementation of the proposed approach enables the manufacturing of structural elements with complex shapes. In particular, the fabrication process allows the final beam to be curved - in the plane containing the longitudinal axis - with variable cross-section heights $h(x)$ (Fig. 1). This beam configuration would require the arrangement of complex (and costly) formwork systems when using classical concrete casting technology (i.e. polystyrene moulds, multiple wooden formworks etc.). A further fundamental characteristic of this approach is that the AM allows the beam to be partially hollow (once it has been properly designed, as explained in the following section), in order to save material, provide functional uses and reduce the final weight, while still guaranteeing adequate mechanical properties related to the intended structural application.

In this study, the approach to produce a curved RC beam is implemented by the 3D printing and subsequent assembling of concrete segments (Fig. 2a). Each beam segment is printed through the thickness of the beam, i.e. in the direction orthogonal to the 2D plane of the beam (z direction in Fig. 1). This allows only cylindrical elements (with equal cross section along the z height) to be printed, with no need to shift the concrete flow layer-by-layer during the printing process to fabricate non-regular shapes through the thickness direction. This is an important point since the low

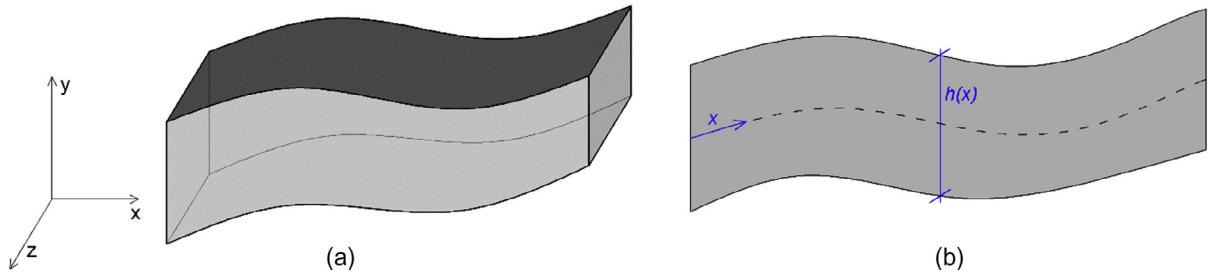

Fig. 1. (a) 3D view and (b) planar section of the target beam with a curved longitudinal axis *x* and a variable cross-section height *h(x)*.

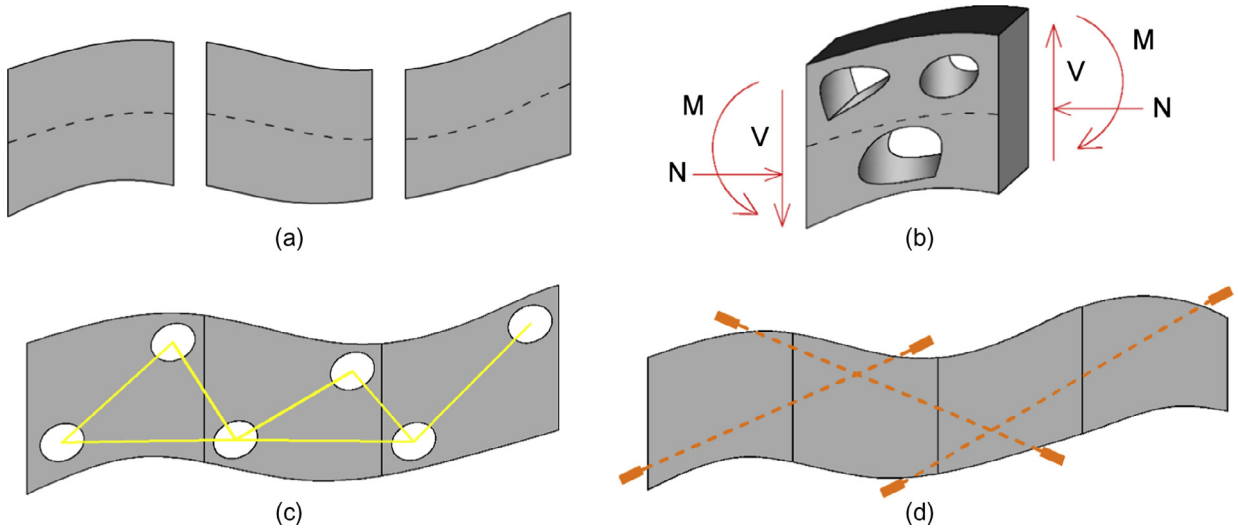

Fig. 2. (a) Possible configuration of the cut "segments" for the target beam; (b) topologically optimized segment with several voids to save materials and guarantee adequate mechanical performances related to the internal forces; (c) rebar reinforcement scheme; (d) post-tensioned cable scheme .

shear strength of the fresh concrete is a major constraint when curved shapes are printed by shifting the layers through the height of the printed element (i.e. cantilevering). In this case, only smooth curved shapes can be fabricated (e.g. see [21], Fig. 2) as a result of the optimization of the printing speed, the flow viscosity, the extrusion force, the layer thickness and other material parameters.

Once the number of segments is defined (mainly depending on printer capabilities), each beam segment is designed to accomplish proper mechanical performances related to the internal forces acting on the beam (shear, axial forces and bending moment). To this end, concrete segments can be topologically optimized with a number of voids, to save material while still guaranteeing the required mechanical performances (see Fig. 2b).

In a second stage, steel rebar reinforcement is installed externally to the beam only after the segments are assembled together by anchoring the steel elements into specific holes made during the printing process (Fig. 2c). To do this, for example, each steel rebar can be bent at both ends to ensure there are two proper anchoring dowels for insertion into the holes. These are then fixed, for examples, with a mortar or structural adhesives. An alternative method consists in a combined in-plane (X-Y) and out-of-plane (Z direction) reinforcement system made of stainless steel threaded rods, as specifically described in Section 2.4. As a result, the steel rebar is designed also to fix the segments together and lock them into a single continuous structural element.

2.2. 3D printing process

Using the approach presented in Section 2.1, we have fabricated two different 3D printed RC beams, being one straight and the other characterized by curved axis and variable cross section along the beam axis itself. The main focus of this sub-section is presenting the features of the printing machine and the printing process itself.

We adopted a BigDelta WASP printer from the Italian CSP company [22] to fabricate concrete segments. The printing area of this machine is a triangle, with each side being about 4.0 m. The printing head is sustained by three braces whose ends are moved along three vertical pillars (Fig. 3). By controlling the movement of the braces, the printing head is moved horizontally and vertically and can reach a maximum height of 1.5 m. The printing head is composed of a conical container with a capacity of about 20 L of fresh concrete. The concrete is extruded by means of a rotating endless screw towards an exit nozzle with a variable diameter. In our case, a 25 mm diameter is used. A control unit guides the movement of the printing head by processing an STL file which includes the layer-by-layer printing paths; Fig. 4a depicts a phase of the printing process of a concrete object. The input parameter to the printer include: the planar path for each layer, the relative height of subsequent concrete layers, and the speed of the printing head (deposition rate).

An optimal balance among those parameters is determined to guarantee that the extruded material could remain stacked, bonded in layers and sustain the weight of the other layers that are deposited on top of each other as the printing process proceeds. In particular, the resulting width of each concrete layer was doubled uniformly in the plane of the printed shape (i.e. obtaining 60 mm of width) by depositing two adjacent path lines; the deposition rate was approximately constant and equal to 20 mm/s, determining an interlayer time gap of approximately 50–90 s depending on the shape of the segment.

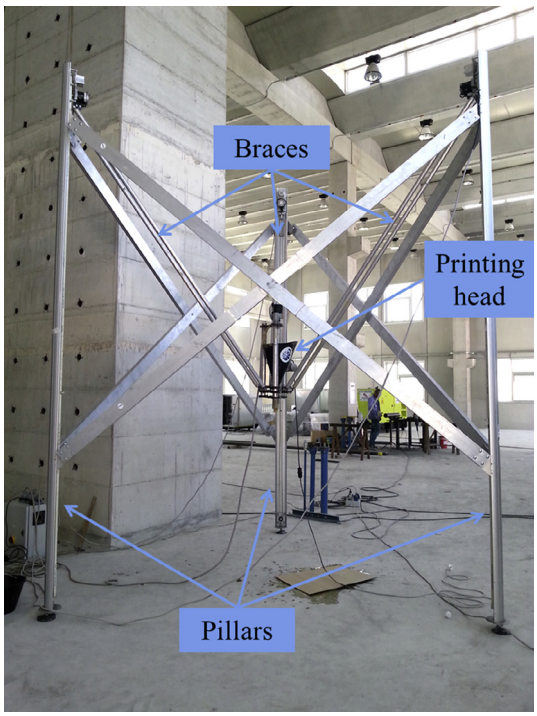

Fig. 3. The printing machine.

2.3. The concrete material

The concrete material is designed to overcome a number of constraints related to the adopted printing process, as following:

- optimal viscosity of the fresh concrete is needed to make it both extrudable, i.e. capable of being ejected through the extrusion head, and buildable, i.e. capable of being stacked in layers.
- high strength is required to compensate for the potential weakness of the connection points between the contiguous layers.
- maximum aggregate size has to be compatible with the extrusion head, the diameter of which is equal to 25 mm.

Given these limitations, a cement-based mortar is fine-tuned with a 0.39 water/cement ratio and a maximum diameter of the aggregates of 4 mm. 0.5% in weight of polypropylene short fibres is also added to the mixture to prevent plastic shrinkage cracking in the early stage of curing and after the deposition process. Nonetheless, since the viscosity of the printing material is affected by the presence of fibres and by the low water/cement ratio, the mix has to be adjusted with a polycarboxylate superplasticizer to achieve an optimal rheological balance with respect to material pumpability. The slump class of the concrete is evaluated according to the EN 12350–2:2009 procedure [23] and is equal to S1, being 14 ± 2 mm the corresponding average slump measure. The average cubic strength R_{cm} of the concrete after 28 days of curing was determined over four specimens and is equal to 53.5 MPa [24]. The average cylindrical strength f_{cm} is estimated as 83% of the cubic strength [27], i.e. 44.4 MPa.

In order to assess whether the printing process affects the material strength in the 3D printed elements, a set of hollow cylinders are designed to be printed and tested under compression along the axial direction. The cross section of the cylinder is designed with one printing line, drawing a circumference with a diameter of 200 mm. The height of the cylinder is equal to 200 mm and composed of 10 layers. Three cylinders are printed with the same process parameters previously described and are shown in Fig. 5. The thickness of the cylinder walls is about 29 mm. The top and bottom surfaces are properly flattened, and the specimens are tested in compression by means of a load controlled machine (Fig. 5a). The average cross section area for each cylinder is computed by means of multiple measures of the external and the internal diameters along the height of the cylinders. The peak force is recorded, and the peak stress is computed over the average cross section area. The average compression strength of the printed cylinders, f_{cpm}, is derived as the average of the peak stress values and is equal to 37.2 MPa. These details are also reported in Table 1. The obtained value for f_{cpm} is lower than the cylindrical bulk strength of the same concrete material, with a reduction equal to 16% of f_{cm}. Besides potential geometrical effects related to the shape of the specimens (i.e. solid vs hollow cylinders) the gap observed in the compressive strengths might also be influenced by two phenomena associated with the printing process: (a) imperfect bond between the layers that can initiate the failure of the specimen, and (b) reduced thickness between adjacent concrete layers (Fig. 5b). These circumstances suggest that a careful evaluation of 3D printed material properties should be considered when designing 3D printed objects with structural features.

2.4. Assembly: straight 3D printed RC beam

In order to avoid possible issues arising from very complex shapes (including experimental test arrangements), as a first

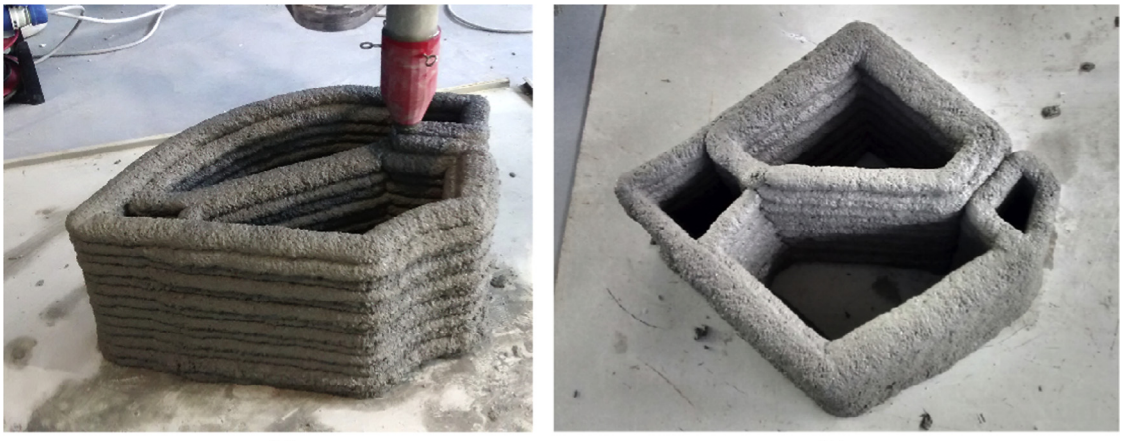

Fig. 4. (a) The printing process and (b) a printed concrete segment.

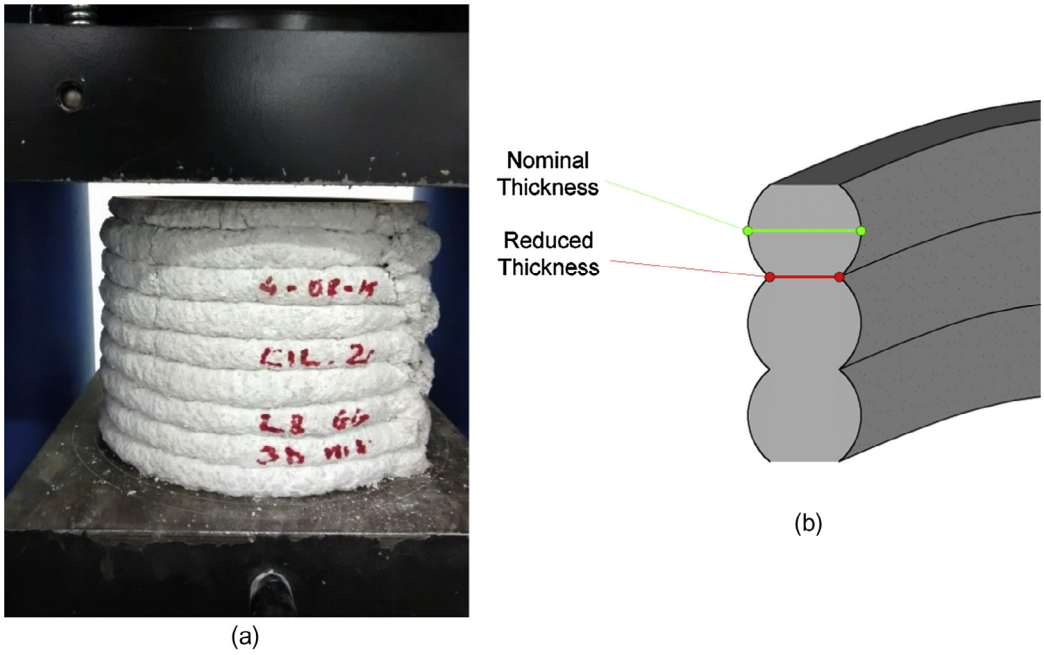

Fig. 5. (a) Printed specimen during the uniaxial compression test; (b) thickness reduction of the printed walls between two contiguous layers.

Table 1
Compression tests on 3D printed cylinders.

Specimen	$D_{ext,ave}$ [mm]	$D_{int,ave}$ [mm]	A_{ave} [mm^2]	F_{max} [kN]	f_{cp} [MPa]	f_{cpm} [MPa]
C1	218	160	17039	594	34.9	**37.2**
C2	218	165	15763	545	34.6	
C3	218	173	13776	579	42.0	

attempt, we have fabricated a straight beam with a constant height by adopting the current AM based approach. This choice is also motivated by the opportunity to easily compare these preliminary results with classical beam theory, while the general approach is still applicable to complex cases. The straight beam is also adopted as specimen in the experimental test.

The target concrete beam is 3.0 m long and characterized by a rectangular cross section with 0.20 m and 0.45 m of width and height, respectively. The 3 m long beam is cut into five segments of two typologies, namely A and B in Fig. 6(a). In detail, with respect to the left side of Fig. 6(a), the type A segment is designed to be installed in its overturned position on the right side of the beam. While the type B, placed in the mid-span, connects the two sides.

According to the procedure, each segment can go through a topological optimization to save as much material as possible and guarantee satisfactory mechanical performances against the internal forces acting on the segment. Furthermore, a number of holes need to be designed to anchor the longitudinal rebar system or, alternatively, install the external shear reinforcing system. It should be pointed out that using external steel reinforcement (rather than embedding it in concrete) might cause corrosion issues due to the direct exposure to the in-service environmental conditions. However, we implement an external steel arrangement as a first attempt to incorporate the reinforcement in the AM-based manufacturing route for RC elements, preventing, either way, corrosion issues by using stainless steel threaded rods in the external reinforcing configuration.

By assuming that a distributed constant load (gravity load) and a concentrated load at the midspan act on the beam, each segment should resist variable bending moments and shear forces. The strut and tie model [25,26] is a rational approach to represent a complex structural member with an appropriate simplified truss system considering all the acting forces simultaneously. Since we want simply to study the flexural behaviour of a straight beam, we decided to adopt such a well-known approach as optimization strategy to design segments A and B. Fig. 7(a) shows the details about dimensions of the two segment types. However, more accurate optimization methods can be used; indeed, topology optimization represents a fundamental step forward for the development of a reliable framework for RC beam printing and will be addressed in following studies by the authors.

The printed segments A and B are shown in Fig. 7(b). Each element is composed of 10 layers with a total height of 20 cm. The diameter of the nozzle is 25.0 mm and the average thickness of the walls is roughly equal to 60.0 mm corresponding to a double thickness-printing path. The beam segments are designed along with the rebar system, to guarantee proper tensile reinforcement (at the bottom side of the beam) and to lock the segments in a single continuous element.

The steel reinforcement scheme adopted in this study is depicted in Fig. 6(b) and is installed on both sides of the beam. It consists in a combined in-plane (X-Y) and an out-of-plane reinforcement system made of stainless steel threaded rods (Z direction) as illustrated in Fig. 8(a). The orthogonal stainless steel threaded rods (Z direction), having a diameter of 12 mm, are positioned into the holes of each module and secured with a high strength low-viscosity cement-based mortar. The stainless steel threaded rods of the in-plane system have a diameter of 16 mm, and are linked to the out-of-plane system through male thread connectors and hex nut rod pipes (Fig. 8b). Table 2 reports technical specification of the connection system constituents. This partic-

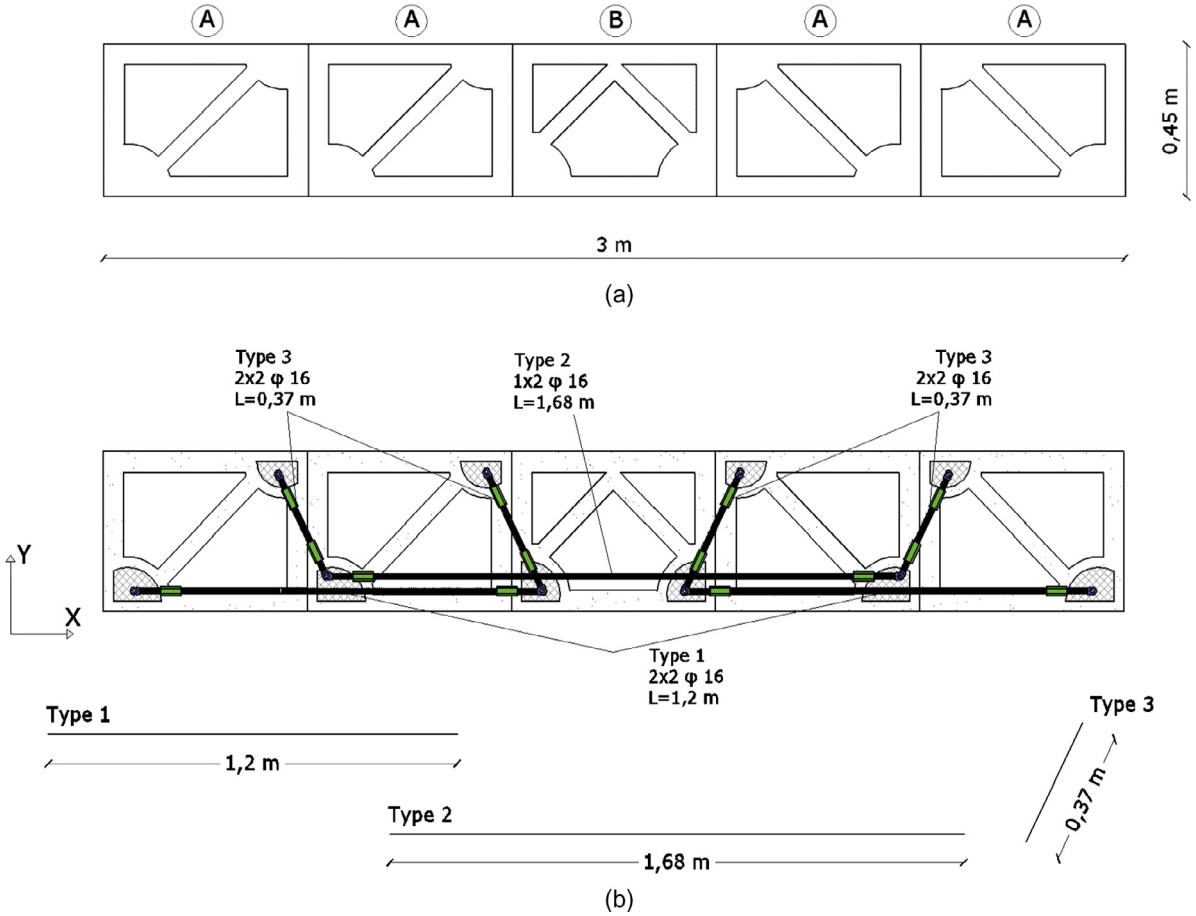

Fig. 6. (a) Target straight beam and geometry of the segments and (b) steel reinforcement scheme.

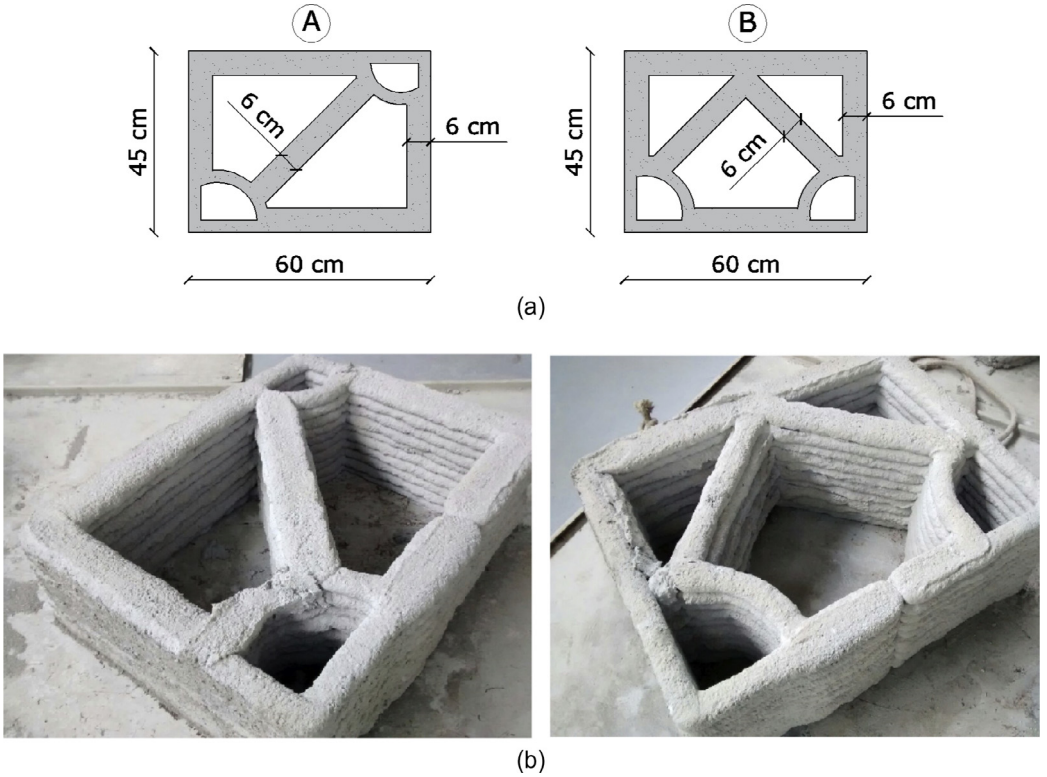

Fig. 7. (a) Schematic representation and dimensions of the beam segments A and B and (b) the correspondent printed segments.

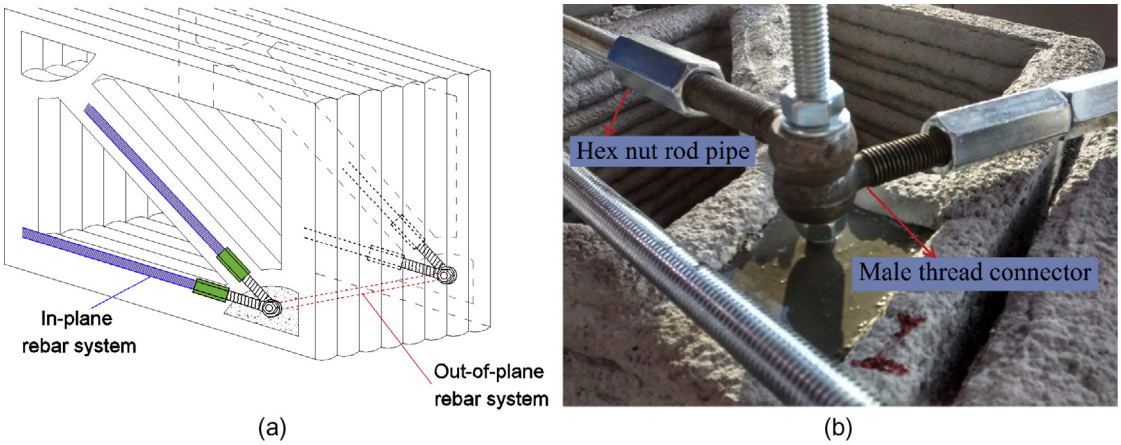

Fig. 8. (a) In-plane and out-of-plane rebar systems; (b) details of the connection system.

Table 2
Technical specification of the connection system constituents.

Male thread connector	M12 × 75 mm UNI 6058, DIN 444
Hex nut rod pipe	M16 × 60 mm UNI 6058, DIN 6334

ular connection system makes possible the assembly and disassembly of the beam thus opening the horizon to the concepts of reusable module or design for deconstruction.

The small grooves between the segments on the top side of the beam are sealed with a low viscosity cementitious mortar to secure the contact between the segments in correspondence with the longitudinal top concrete chord.

The beam segments and the rebar system are designed to provide a final element with the following features:

- a top continuous concrete chord to bear the compression forces induced by the flexural behaviour;
- a bottom steel chord to balance the top compression stresses and bear the tensile forces;
- diagonal compression concrete struts and opposite diagonal steel struts in the lateral segments to bear the shear forces.

The total weight of the beam is 36 kN, which is about 12 kN/m of distributed weight. This equates to about 54% of the weight of the equivalent solid beam, the cross section of which has the same overall dimensions, i.e. 0.20 m × 0.45 m.

2.5. Assembly: curved shape beam

A second 3D printed beam has been also produced and consists in an irregular arc (longitudinal profile of Vesuvius volcano) of about 4.00 m long with a transverse width equal to 0.25 m. The whole shape is characterized by a double path line of printed concrete with the exception of the hole edges (Fig. 9). The rebar connection system is the same adopted for the straight RC beam.

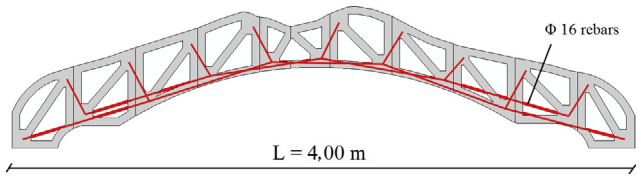

Fig. 9. Geometric configuration of the curved shaped 3D printed RC beam.

Such an irregular shape has been chosen to exploit the potentialities of AM opportunities, consisting in 3D printing of freeform concrete elements with respect to traditional manufacturing techniques. In fact, as it can be noticed from Fig. 9, each 3D printed concrete segment is different from the others without the constraint of producing pieces with the same shape.

The final configuration of the printed beam is depicted in Fig. 10. In this preliminary phase of the work, we have optimized the shape of each beam segment according to the numerical estimation of internal stress distribution for a similar arch-shaped solid concrete beam. This allows the "ideal" removal of concrete material from the solid beam configuration, still guaranteeing proper segment strength and stiffness properties. The experimental assessment of the mechanical properties of such a beam is out of the scope of this study and will be considered in future works by the authors.

2.6. Flexural behaviour assessment of the straight 3D printed RC beam

To evaluate the flexural behaviour and failure mechanisms of the straight 3D printed RC beam manufactured following the proposed approach, both an experimental test and numerical analyses are performed. In the present sub-section, we illustrate the experimental set-up for the three-point bending test conducted on the RC straight beam and the corresponding 2D numerical model built with the software SAP2000.

2.6.1. Experimental set-up

The straight 3D printed RC beam described in Section 2.4 is considered as specimen for a three-point bending test. The test is carried out by means of a universal servo-hydraulic testing machine with 500 kN force capacity while the load scheme is set to ensure that the primary failure comes from tensile or compression stress. This is done by minimizing the shear stresses arising from the test thus by controlling the shear span to depth ratio [27], i.e., the length of the outer span divided by the height (depth) of the specimen. The test is conducted under displacement control with a velocity of 0.5 mm/min.

Strain measurements on the steel components of the beam are achieved through fourteen (seven for each side of the beam) strain gages placed at half-length of each stainless threaded rod, as illustrated in Fig. 11. For the strain measurements of compressed concrete, nine strain gages are installed only in the backside of the beam (see Side B of Fig. 11). The backside of the beam is made

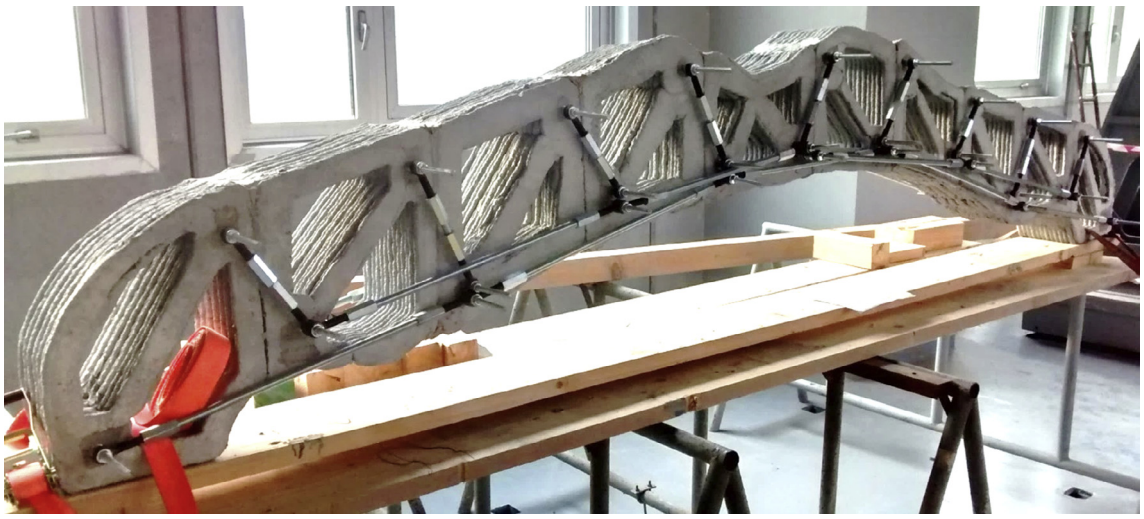

Fig. 10. 3D printed RC beam with a variable cross section.

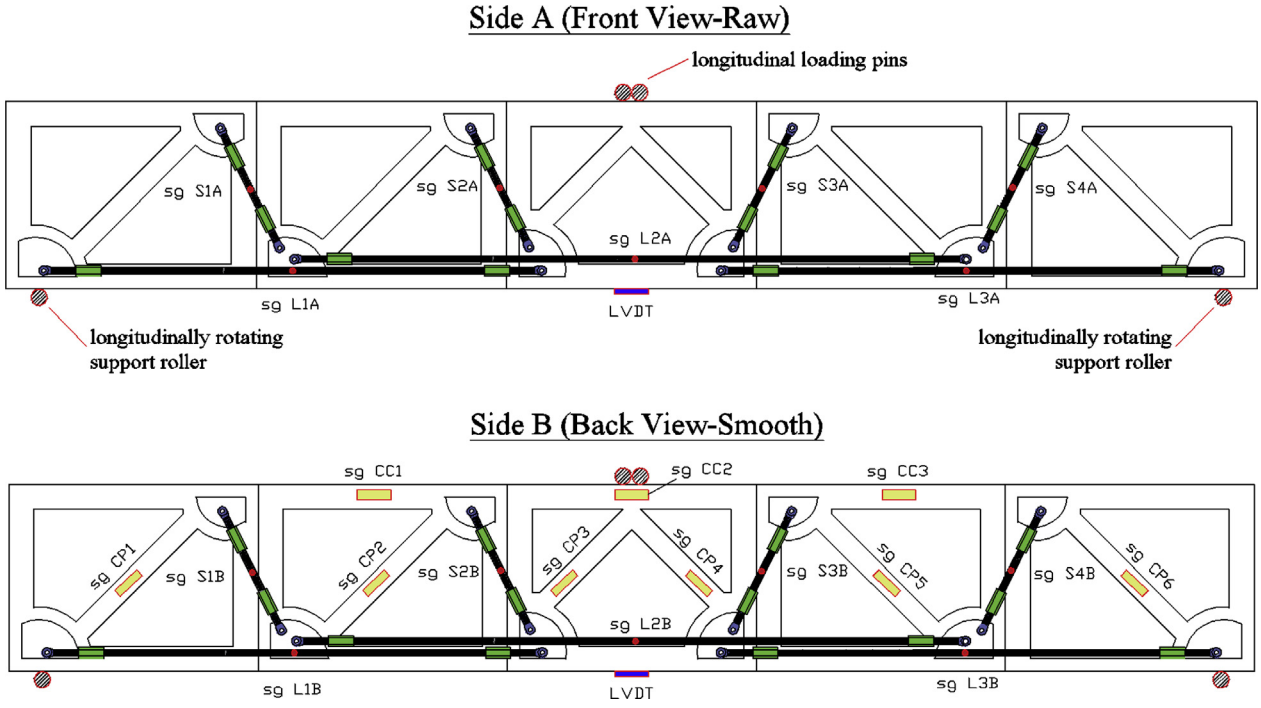

Fig. 11. Front view and back view of the straight beam with strain measurement devices: strain gages for steel rods (red circles), concrete chord/struts (yellow rectangles) and LVDTs (blue rectangle) for the measurement of displacements at the beam mid-span. (For interpretation of the references to colour in this figure legend, the reader is referred to the web version of this article.)

smooth on purpose in order to ensure the grip between the concrete surface and the strain gages. To measure the displacement at the mid-span of the beam, two linear variable differential transducers (LVDTs) are placed at the bottom edge in correspondence of the half of the beam.

The load-displacement curve is obtained digitally as the test proceeds, while, at the same time, the strain-displacement curves for all the strain gages applied on the steel rods and on the concrete chords are recorded. Fig. 12 shows the final arrangement of the beam specimen for the three-point bending test.

2.6.2. Numerical modelling

A finite element (FE) model of the straight 3D printed RC beam is also built up in order to interpret the experimental results we present in the next section. To reduce computational costs, a simplified 2D model is built with the software SAP2000 [28], choosing 1D-frame elements for the discretization of the beam system (see Fig. 13). The black points represent the nodes defining the elements, thus, the model discretization. The beam is modelled considering only half of the geometry, applying and ideal symmetric cutting plane (X-Y) at half width of the beam (Z direction). In this way, it is possible to build a 2D model and consider only one side of the beam thanks to the symmetry of the reinforcement system. Such a simplified modelling can be considered enough accurate also because the actual beam is nearly a strut and tie system, consisting of diagonal compression concrete struts and opposite diagonal tension steel ties. Furthermore, to model the interface connection between the surfaces of two adjacent segments, we define another set of frame elements with suitable elastic properties, called *link elements* and numbered in Fig. 13.

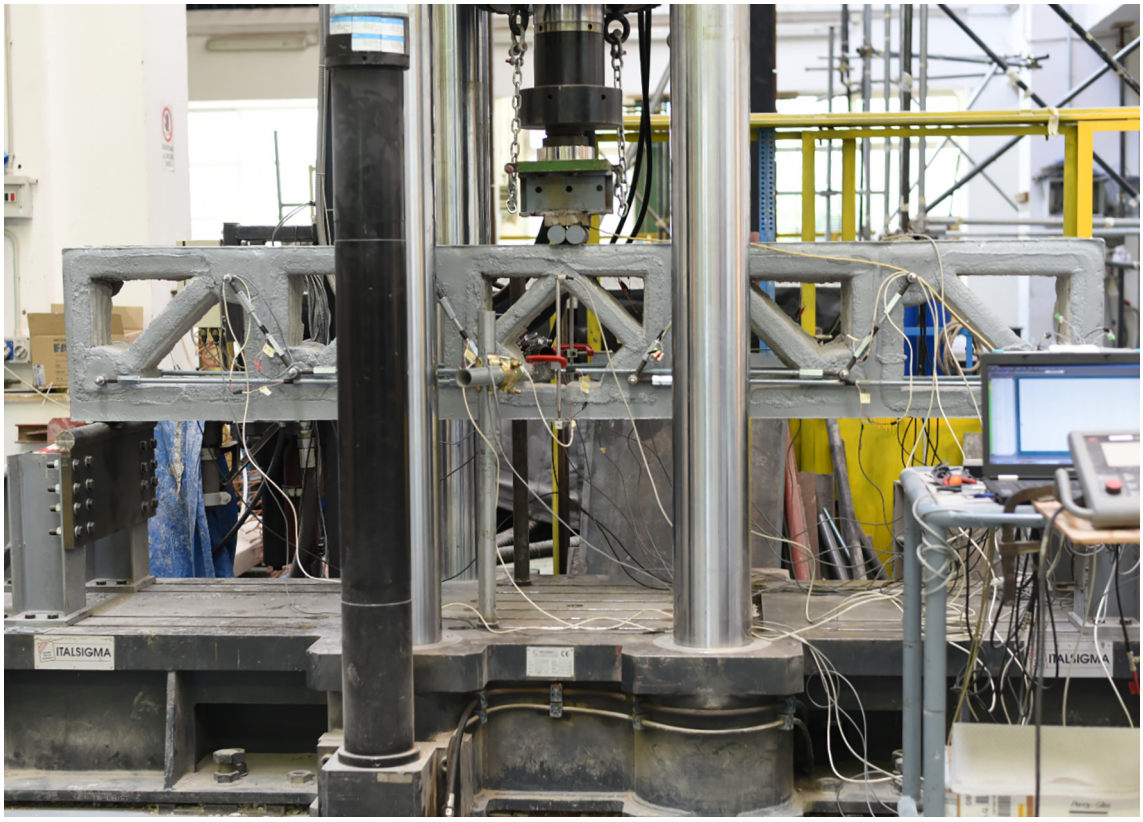

Fig. 12. Equipped specimen for the three points bending test.

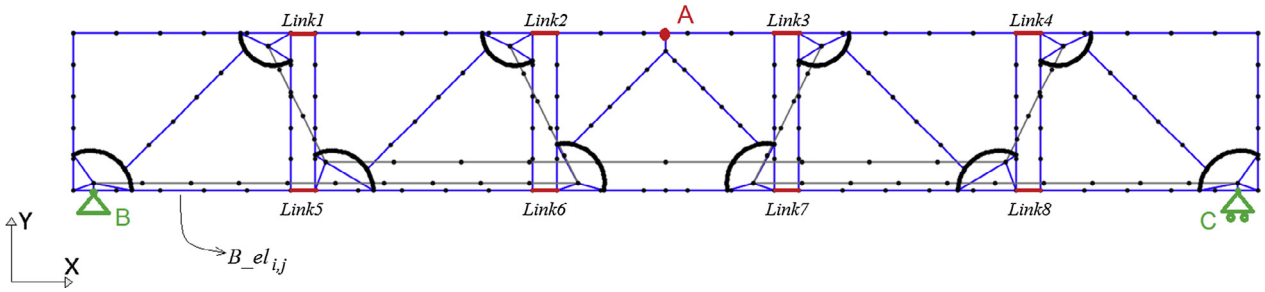

Fig. 13. FE model details and boundary conditions for the straight RC beam. The *link elements* are introduced to model the interfaces between adjacent concrete segments. ***B_el*$_{i,j}$** notation refers to finite elements of the concrete bottom chord, where *i* indicates the concrete segment (1–5) and *j* indicates the number of the element enumerated with increasing order from left to right.

We also introduce the notation $B\_el_{i,j}$ (see Fig. 13) to identify the generic frame element of the concrete bottom side, where *i* indicates the concrete segment to which it belongs (as an example, *i = 1* identifies the first concrete segment starting from left of Fig. 13) and *j* indicates the number of the element enumerated with increasing order from left to right.

A CAD software is used to draw the actual beam geometry (after printing stage) and then imported in SAP2000. At this stage, we define cross-sections and corresponding properties to be assigned to the frame elements. Frame properties are chosen in accordance with the real dimensions measured on the beam (for the concrete segments) and the diameters adopted for the tethered rods.

The following boundary conditions are applied to the 2D beam model (see Fig. 13):

1. out-of-plane displacement constrained (UZ = 0) at each node of the mesh;
2. all displacements and rotations around X and Y constrained (UX = UY=UZ = RX=RY = 0) at point B;
3. out-of-plane and vertical displacements and rotations around X and Y constrained (UY = UZ=RX = RY=0) at point C;
4. concentrated load applied at point A;
5. Gravity load in the vertical (Y) direction applied at each node of the mesh.

Material properties are defined as in Table 3 for concrete and steel, respectively. The numerical simulations are carried out

Table 3
Material properties assigned to the frame sections.

Concrete	Steel
E = 30000 MPa	E = 210000 MPa
υ = 0.2	υ = 0.3

according to the actual experimental evolution of the above-described three-points bending test, in order to achieve a satisfactory correspondence with the three-point bending test results. Specifically, in such a simplified analysis, the FE model configuration is modified in accordance with the development of the cracking process, by removing one or more *link* elements and frame elements which do not react anymore to traction, or degrading material properties of the link themselves. For all the resulting models, a linear static analysis has been performed. This choice comes from the fact that the beam system tested in this study does not exhibit a clear non-linear behaviour from the material point of view, rather the nonlinearity depends on the assembly configuration under loading, as will be better demonstrated in the experimental results section.

3. Results and discussion

The results of the experimental test and numerical analyses carried out on the straight 3D printed RC beam are included in this section. Comparisons between experimental and numerical data are presented in order to validate numerical simulations as well as to obtain a better interpretation of the experimental test.

3.1. Experimental results

In this section, we analyse the experimental outcomes obtained from the three-points bending test carried out on the straight 3D printed RC beam. In terms of overall flexural behaviour, it is possible to identify two main mechanical stages from the load-deflection curve reported in Fig. 14: a *linear elastic stage*, in which the beam is intact (nor cracked or disassembled) and a *non-linear stage*, in which local/global cracks occur or interface failure takes place. The *non-linear stage* can be itself subdivided into *start of cracking stage* (curve between A-B points) and *progression of cracking stage* (curve between B-C points) until the final *failure stage* (curve from point C) corresponding to the complete loss of load carrying capacity of the beam.

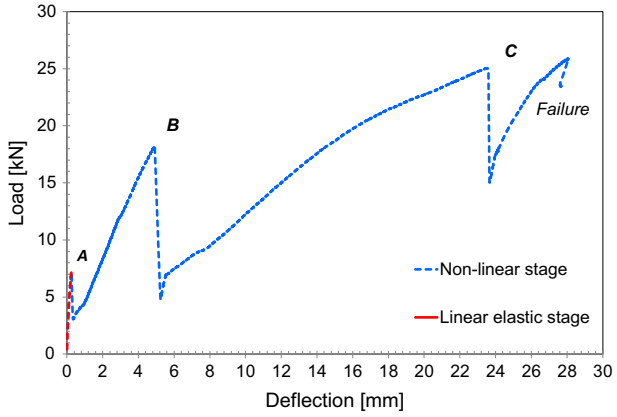

Fig. 14. Linear elastic and non-linear stages of the load-deflection curve from experimental data.

To facilitate the understanding of the cracking/failure mechanisms developed by such system, Fig. 15 shows the sequential order of crack creation and propagation along the beam.

The formation of the first tensile crack in the concrete (bottom side) corresponds to the point of transition from the *linear elastic stage* (in which the beam is intact) to the *non-linear stage*, as depicted in Fig. 16 (a) and identified in the load-deflection curve of Fig. 14, Point A. This first brittle failure occurs at the bottom side of the concrete segment adjacent to the mid one for a load level of approximately 7 kN. This transition corresponds to a moderate loss of carrying load capacity and is associated to the reduction of the cross-sectional area of the concrete segment undergoing cracking. After the transition from the linear to the non-linear stage, the load increases with an almost linear branch until the formation of the second major crack which is identified with the second peak in the Force vs Deflection curve (point B) corresponding to an applied load of about 18 kN. Even if the flexural behaviour is considered as non-linear between points A and B (*start of cracking stage*), the Force vs Deflection curve still maintains a linear slope as the first part of the curve. Indeed, the first two cracks at the concrete bottom side lead to an initial loss of stiffness but, at the same time, the beam system is still reacting as a continuous element because the connection between the steel reinforcements and the concrete segments is preserved. Fig. 16(b) shows a detailed view of the second crack formation.

A different trend can be noticed in the shape of the force-displacement curve between points B and C, in which *progression of cracking stage* occurs, exhibiting a non-linear behaviour. Besides the growth of the existing cracks (nr. 1 and 2), in this stage it is possible to recognize the formation of three further major cracks (3rd, 4th and 5th crack in Fig. 16c) localized between the first and the second concrete segment. During this loading stage, the three major cracks did not develop in a distinct or sequential manner, making not possible to clearly identify which one of them determines the third peak load (point C) and the corresponding drop in the load-deflection curve. Furthermore, the mechanism of fracture developed in this stage increases in complexity, involving the bottom side of 1st and 2nd concrete segments (tensile cracks), the interface connection surface between the same concrete segments (interface opening and relative sliding), and the connection system between the steel reinforcement and the concrete (shear failure of the anchoring substrate made of concrete material).

The final part of the Force vs Deflection curve (from point C until final failure) is representative of the *failure stage*. In detail, after reaching of the ultimate peak load of approximately 25 kN, severe damage occurs in correspondence of the connection system between the steel reinforcement and the concrete segment adjacent to the mid one (see Fig. 16d). This circumstance is responsible for the global failure of the beam.

Finally, it is worth making some considerations about the magnitude of the deflection at failure recorded in the flexural test. As shown in Fig. 14, the maximum value of the deflection is quite

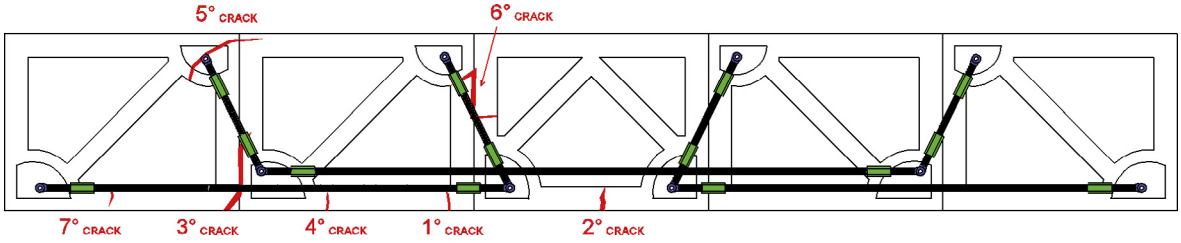

Fig. 15. Sequential order of crack formation during the test.

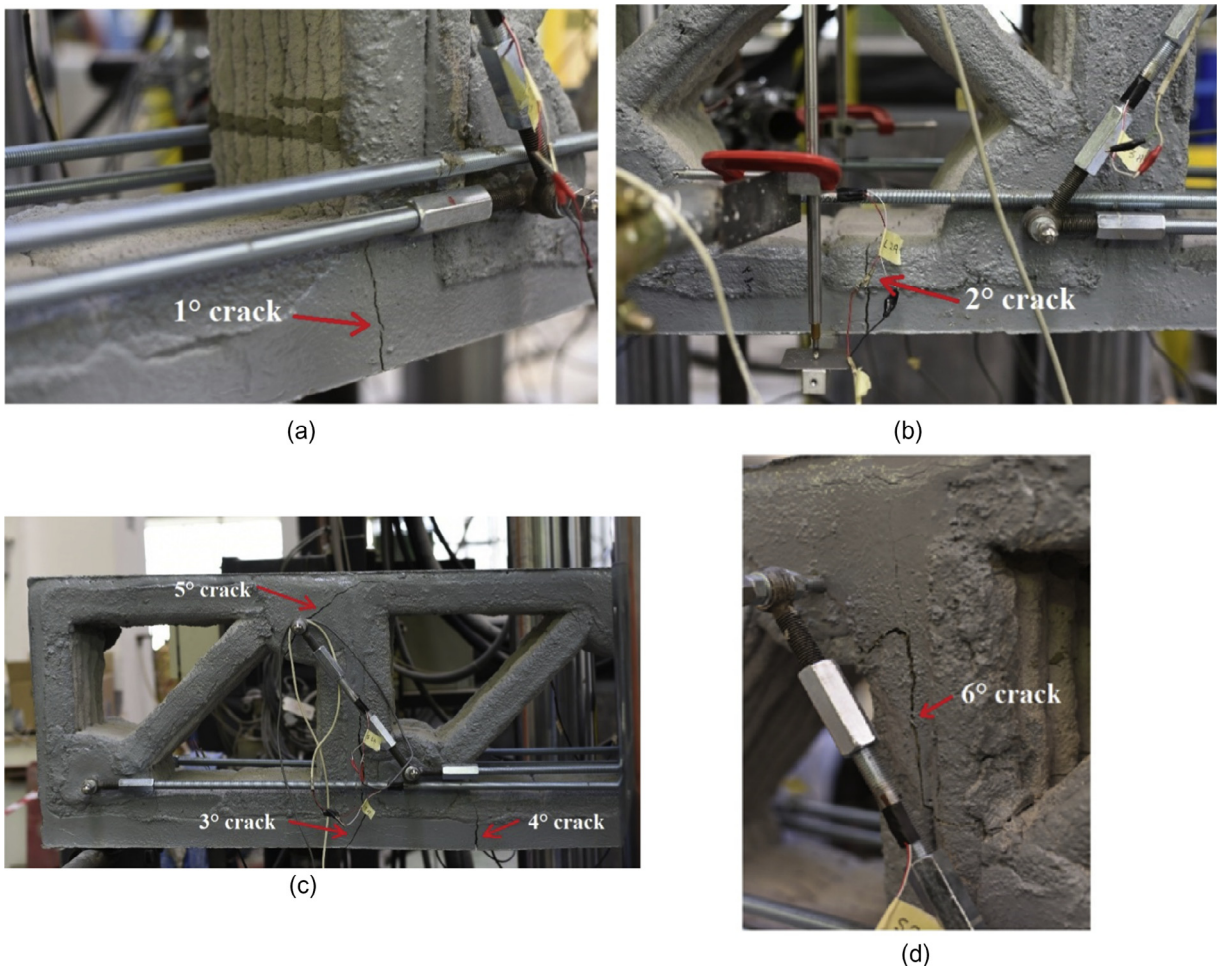

Fig. 16. (a) 1st crack; (b) 2nd crack; (c) front view of the 3rd, 4th and 5th cracks; (d) 6th crack (d).

large if compared with that of a generic standard solid RC beam, especially since the steel rebars have not even reached the yielding limit. Nevertheless, looking at the *linear elastic stage*, the behaviour of the 3D printed beam is satisfactory, being the level of flexural deflection comparable with an equivalent solid RC beam but associated with a significant weight reduction. On the contrary, for the *non-linear stage*, the loss of stiffness (and, consequently, large deflections) derives mainly from the low effectiveness of the connection/interface system (as the flexural load increases) rather than from the reduction of the material properties or a wrong segment optimization strategy. For this stage, it would be worthy to draw a parallel with the displacements associated with the ductile region of an equivalent solid RC beam; however, due the different nature of the failure behaviour (connection system vs material ductility), this aspect deserves more attention and is currently under investigation by the authors.

From the strain measurements recorded during the flexural test, it has been noticed that the yielding limit in the stainless steel threaded rods (i.e. approximately 0.18%) is never attained upon ultimate beam failure. This is clearly observable in Fig. 17 where we report the tensile strain vs deflection curve recorded by the L2A and L2B strain gages (see Fig. 11) which are applied to the tethered rods in correspondence of the mid-span of the beam, i.e. the steel elements undergoing major tensile stresses. In addition, concrete material belonging to the upper compressed side of printed segments does not experience any permanent failure given that the strain levels do not exceed non-linear limits (i.e. approximately 0.20%).

Overall, the experimental outcomes revealed that the proposed RC beam system based on AM technology is prone to local damage phenomena occurring as flexural load increases. Besides moderate loss of stiffness related to cracking of concrete under traction, the major limitation relies on the concrete segment assembly which can suffer from local failure mechanisms driven by shear forces arising at the interfaces between segments themselves. In addition, the low tensile strength of concrete material in correspondence of the upper anchoring of steel stirrups may play as a further brittle

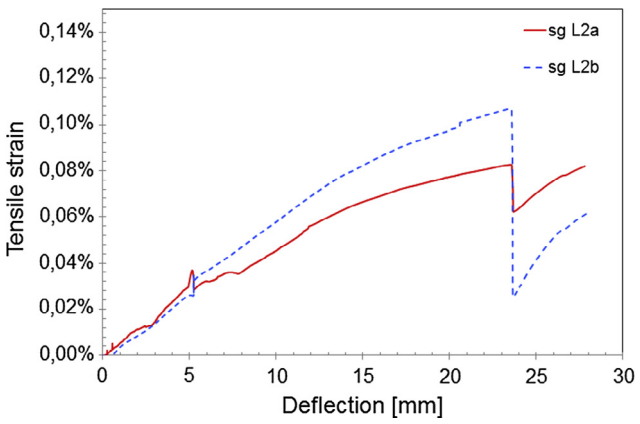

Fig. 17. Tensile strain-deflection curve registered by the L2a and L2b strain gages applied on the steel bars.

damage mechanism which triggers disconnections among components. Consequently, this characteristic behaviour can be assumed as non-linear as a consequence of the above mentioned progressive failure mechanisms. Possible solutions to this issue are discussed in the Conclusion section.

3.2. Numerical results

The results of the numerical analyses are presented in this section in order to better understand the failure mechanisms and the linear/non-linear stages observed in the experimental Force vs Deflection curve. The analyses are also aimed to reproduce the characteristic stages of the flexural response of the beam observed during the progression of cracking formation. Three of four main stages identified during the experimental test (*linear elastic stage, start of cracking stage*, *progression of cracking stage* and *failure stage*) correspond to three different FE models constructed by modifying the model configuration described in the Numerical analysis section (i.e. changing frame element and the connection properties among segments).

Starting from *the linear elastic stage*, Fig. 18 shows the experimental load-deflection curve (blue line) measured at the mid-span of the beam compared with that obtained from numerical simulation (named as Numerical 3D Printed_Stage1 curve, red line). In this latter case, the FE model of the beam comprises all the frame and link elements showed in Fig. 13 having the standard material properties of Table 3. The comparison with an equivalent performance of a standard RC beam is made only for the linear elastic stage. The reason lies in the very different failure modes observed for the printed beam (i.e. no steel yielding) and the significant difference in the amount of concrete utilized that would have made an overall comparison complex to interpret. Accordingly, in the graph of Fig. 18 we consider the Force-Displacement curves corresponding to the non-cracked (black dotted line) and the cracked (green dotted line) configuration of a full solid RC beam with the same overall cross-section dimensions of the printed RC beam (i.e. 45 cm × 20 cm); in the latter case, the cross section of the equivalent RC beam refers to that after first concrete cracking. In terms of overall flexural stiffness, the FE model (Numerical 3D Printed_Stage1 curve) reproduces satisfactorily the experimental Force vs Deflection curve in the elastic range. Moreover, it is noticed that the flexural behaviour of the 3D printed RC beam is intermediate between that of the Equivalent Solid Beam and the Equivalent Cracked beam.

The second main stage of the force-displacement curve, noticeable from the three points bending test, corresponds to the non-linear response of the beam system. Fig. 19 reports the overall load-deflection curve recorded during the test and the overlapped curves obtained from the FE numerical simulations. Before going into the details of numerical-experimental comparison, it is worth pointing out that some adjustments are made to the initial FE model on the basis of the experimental evidence of crack progression observed in the stages AB and BC of Fig. 19. In detail, the Numerical 3D Printed_Stage2 curve of Fig. 19 is obtained by removing *Link6*, $\boldsymbol{B\_el}_{3,3-4}$ and $\boldsymbol{B\_el}_{2,5}$ elements (see Fig. 13) from the initial FE model (named as Numerical 3D Printed_Stage1). Those elements are considered as mechanically not reacting in the stage AB on account of the fact that 1st and 2nd cracks occurred in the 3D printed beam (see Fig. 15) at point A of the Force vs Deflection curve. Starting from this adjusted FE model, the Numerical 3D Printed_Stage3 curve is obtained by further removing *Link5* and $\boldsymbol{B\_el}_{1,5}$ element (see Fig. 13) because of the formation of the 3rd-5th cracks (see Fig. 15) at point B of stage BC. As consequence of the crack pattern, also the material properties assigned to the link elements correspondent to the interface area subjected to the cracking phenomena are properly degraded.

Focusing on the *start of cracking stage*, as already underlined in the experimental results section, the behaviour becomes globally non-linear due to force drops in the experimental force vs deflection curve; however, the curve between points A-B still maintains a linear slope which matches well with the numerical model (Numerical 3D Printed_Stage2).

Focusing on the experimental curve between B-C points, corresponding to the *progression of cracking stage*, the numerical curve (Numerical 3D Printed_Stage3) matches quite well the experimental one until a load value of around 15 kN; afterwards, the numerical curve slightly diverges from the experimental one. The worsening in the response prediction through the numerical model can be explained analysing the evolution of the cracking process. The local effects induced by the new crack mechanism lead to an emphasised non-linear trend in the experimental data not captured by the simplified numerical model. Indeed, the formation of the 3rd–5th cracks is the result of the tensile failure of the concrete at the bottom side of the beam, the sliding at the interface surface between adjacent concrete segments, and the shear failure of the steel anchoring system.

Fig. 20 reports the contour plot of the axial stress component obtained from the Numerical 3D Printed_Stage1,2,3 analysis. Fig. 20(a) shows the level of traction stresses corresponding to the Numerical 3D Printed_Stage1. Here, the top concrete chord is under compression loads while the bottom chord of the beam is under traction with axial stresses of the order of approximately

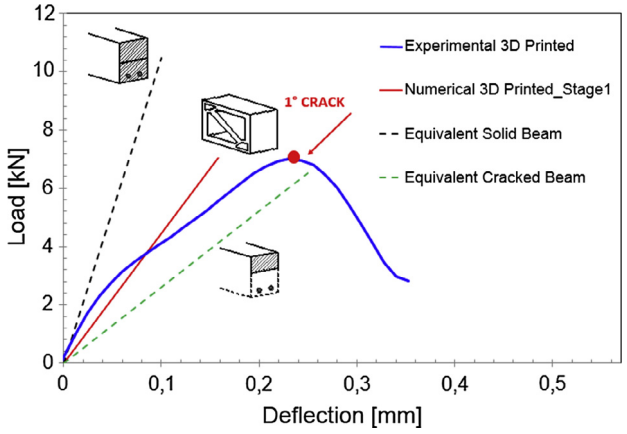

Fig. 18. Linear elastic stage: load-deflection curves from experimental data and simulations.

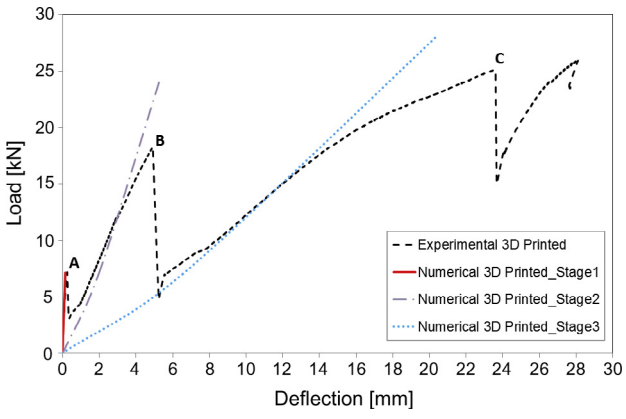

Fig. 19. Load-deflection curves from experimental data and simulations.

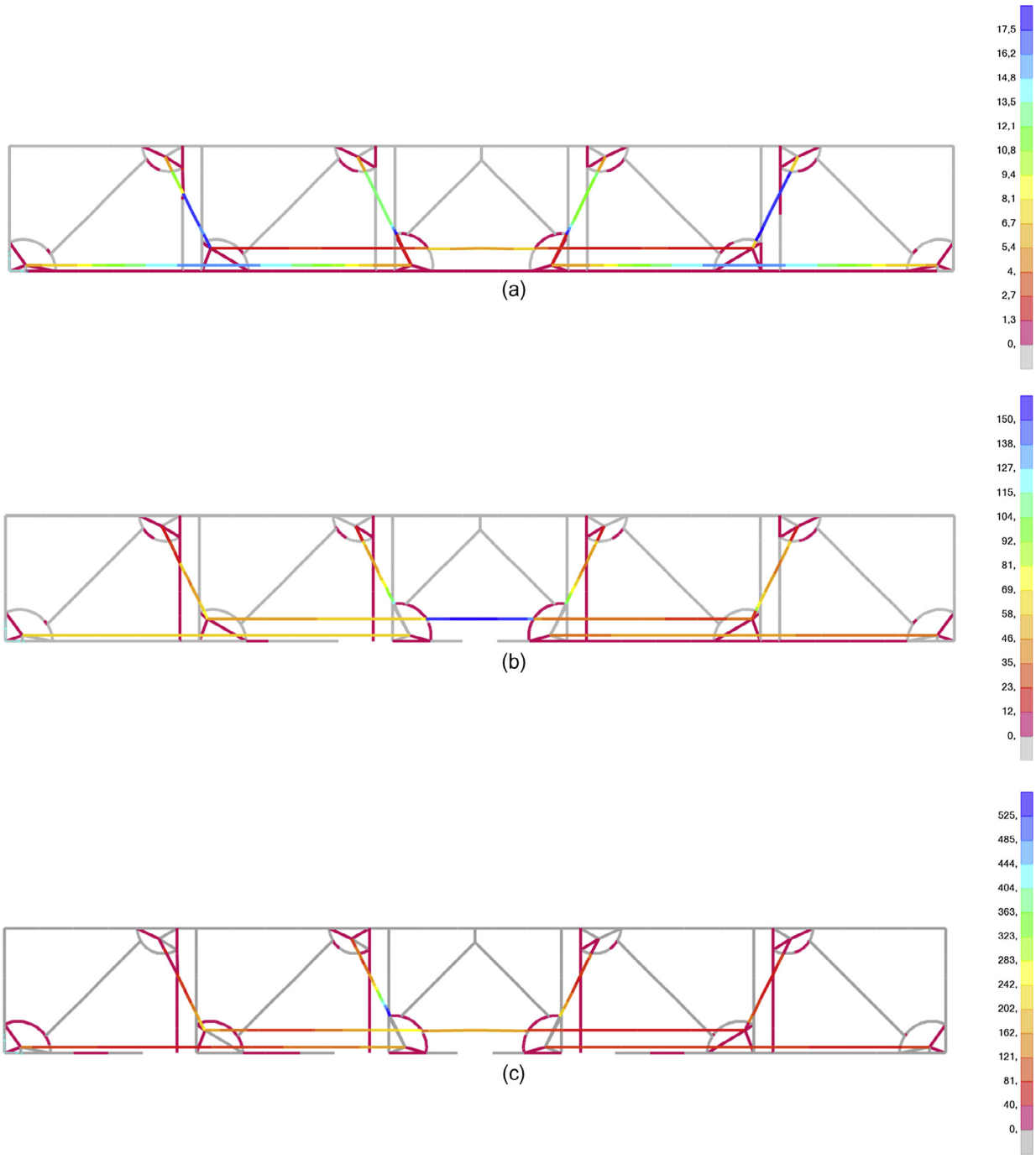

Fig. 20. (a) Contour plot of the axial stress component (traction stresses are showed in a colored contour) σ_{11} obtained from: numerical 3D Printed_Stage1, (b) numerical 3D Printed_Stage2 and (c) numerical 3D Printed_Stage3.

1 MPa, close to the cracking limit of the concrete under traction. The reinforcement system is also subjected to traction even if the values observed are very low. The FE simulation also highlights how the 3D printed beam systems behaves as a strut-tie ideal model, consisting of concrete compression members (i.e., struts) and steel tension members (i.e., ties).

Fig. 20(b) shows the level of stress correspondent to the Numerical 3D Printed_Stage2, where the first cracks come into play. Here, all the steel rebars of the reinforcement system remain loaded, while it is possible to notice some concrete elements undergoing traction stresses at the anchoring sites of the transverse steel reinforcement. The traction in the upper part of the beam is related to the development of the failure mechanism mainly localized between concrete segment 2 and 3; in any cases, the stress level in those elements correspond to values around 0.5 MPa. Furthermore, as the concrete links are removed following first cracking, the traction stresses in the bottom chord are redistributed amongst the other segments.

The contour plot in Fig. 20(c) refers to the to the Numerical 3D Printed_Stage3 and to a vertical concentrated force of 27 kN which almost corresponds to the beam failure load level. At this stage, mostly all the bottom concrete elements are not subjected to traction stresses due to the stress redistribution after progressive cracking. The stress concentration between concrete segment 2nd and

3rd is particularly reflected in the steel reinforcement response, in correspondence of which the rebars are the more stressed ones (even if never reaching the yielding limit, in accordance with the strain-deflection curve recorded by the strain-gages, see Fig. 17). The local damage mechanism also determines a stress concentration in the steel stirrup connection system between the 2nd and the 3rd concrete segment (approximately 450 MPa). All the diagonal concrete struts are in compression as expected.

Focusing on Fig. 19, the final part of the curve (from point C until the failure) describes the *failure stage*. The prediction given by the simplified numerical model is considered useless for this portion of the curve, due to the considerations about the complexity of the failure mechanisms.

4. Conclusion

In this study, a novel approach to fabricate RC members by assembling 3D printed concrete segments has been presented and discussed. A first application of this technology has been proved in practice by fabricating and testing under flexural load a 3.0 m long RC beam. The preliminary outcomes of an experimental activity have been illustrated and discussed. The initial flexural stiffness of the printed RC beam has resulted comparable with an equivalent full solid RC beam whereas the overall nonlinear flexural behaviour has been influenced by local failure mechanisms, i.e. shear damage at the interfaces between adjacent concrete segments and steel-concrete anchoring failure. The overall deflection has resulted large due to the mentioned damage mechanisms, limiting the overall performances of these elements; indeed, even though large deflections have been observed, no steel yielding was recorded in the external reinforcement system. A numerical finite element model has been implemented to reproduce the characteristic flexural response of the printed beam in terms of stresses produced in the concrete segments and steel components. The resulting stress distribution highlighted the major role played by interfaces and connections during flexural loading. For this reason, more investigations are needed to further address some critical issues and extended this approach to innovative practical cases. Among the issues, overall ductility, comparison with standard performances, size effects related to the printed technology, environmental degradation, steel rebar embedment and fire resistance may represent further topic of interest for such a technology. Nevertheless, the authors want to emphasize that the basic idea herein presented can introduce a novel rational use of AM technologies in structural engineering as it enables the fabrication of complex shapes (e.g. curved beams of variable heights), the topological optimization of shapes, the reduction of concrete volume and mass, the elimination of complex formwork systems, the easy transportability and installation.

Acknowledgements

Authors want to acknowledge the consortium STRESS s.c.a.r.l. for supporting this activity and in particular Marco Iuorio, Marcello Pellecchia and Alberto Zinno. Authors also thank Marco Naclerio and Luigi Frascogna from the University of Naples Federico II.

References

[1] ASTM. "ASTM F2792-10 Standard Terminology for Additive Manufacturing Technologies." American Society for Testing and Materials (ASTM)
[2] B. Berman, 3-D printing: the new industrial revolution, Bus. Horiz. 55 (2) (2012) 155–162.
[3] H. Lipson, M. Kurman, Fabricated: The New World of 3D Printing, John Wiley & Sons, 2013.
[4] F. Rengier, A. Mehndiratta, H. von Tengg-Kobligk, C.M. Zechmann, R. Unterhinninghofen, H.U. Kauczor, F.L. Giesel, 3D printing based on imaging data: review of medical applications, Int. J. Comput. Assisted Radiol. Surg. 5 (4) (2010) 335–341.
[5] T. Campbell, C. Williams, O. Ivanova, B. Garrett, Could 3D Printing Change the World, Technologies, Potential, and Implications of Additive Manufacturing, Atlantic Council, Washington, DC, 2011.
[6] J.-P. Kruth, G. Levy, F. Klocke, T.H.C., Childs Consolidation phenomena in laser and powder-bed based layered manufacturing, CIRP Annals – Manuf. Technol. 56 (2) (2007) 730–759.
[7] U. Scheithauer, E. Schwarzer, H.J. Richter, T. Moritz, Thermoplastic 3D Printing—An additive manufacturing method for producing dense ceramics, Int. J. Appl. Ceram. Technol. 12 (1) (2015) 26–31.
[8] C. Ladd, J.H. So, J. Muth, M.D. Dickey, 3D printing of free standing liquid metal microstructures, Adv. Mater. 25 (36) (2013) 5081–5085.
[9] J.A. Inzana, D. Olvera, S.M. Fuller, J.P. Kelly, O.A. Graeve, E.M. Schwarz, H.A. Awad, 3D printing of composite calcium phosphate and collagen scaffolds for bone regeneration, Biomaterials 35 (13) (2014) 4026–4034.
[10] R.A. Buswell, R.C. Soar, A.G. Gibb, A. Thorpe, Freeform construction: mega-scale rapid manufacturing for construction, Autom. Constr. 16 (2) (2007) 224–231.
[11] Timothy Wangler et al., Digital concrete: opportunities and challenges, RILEM Tech. Lett. 1 (2016) 67–75.
[12] B. Khoshnevis, Automated construction by contour crafting-related robotics and information technologies, Autom. Constr. 13 (1) (2004) 519.
[13] S. Lim, R.A. Buswell, T.T. Le, S.A. Austin, A.G. Gibb, T. Thorpe, Developments in construction-scale additive manufacturing processes, Autom. Constr. 21 (2012) 262–268.
[14] A. Tibaut, D. Rebolj, Interoperability requirements for automated manufacturing systems in construction, J. Intell. Manuf. (2014), https://doi.org/10.1007/s10845-013-0862-7.
[15] E. Lloret, A.R. Shahab, M. Linus, R.J. Flatt, F. Gramazio, M. Kohler, S. Langenberg, Complex concrete structures: merging existing casting techniques with digital fabrication, Comput. Aided Design 60 (2015) 40–49.
[16] I. Perkins, M. Skitmore, Three-dimensional printing in the construction industry: a review, Int. J. Constr. Manage. 15 (1) (2015) 1–9.
[17] S. Austin, S. Lim, T. Le, Mix design and fresh properties for high-performance printing concrete, Mater. Struct. 45 (8) (2012) 1221.
[18] M. Sakin, Y.C. Kiroglu, 3D printing of buildings: construction of the sustainable houses of the future by BIM, Energy Proced. 134 (2017) 702–711.
[19] H. Valkenaers, D. Jansen, A. Voet, A. Van Gysel, E. Ferraris, Additive manufacturing for concrete: a 3D printing principle, in: Proceedings of the 14th euspen International Conference, 2014, vol. 1, pp. 139–142.
[20] A. Perrot, D. Rangeard, A. Pierre, Structural built-up of cement-based materials used for 3D-printing extrusion techniques, Mater. Struct. (2015) 1–8.
[21] http://www.totalkustom.com/ visited on 2015/08/12
[22] http://www.wasproject.it/ visited on 2015/08/12
[23] EN 12350, Testing fresh concrete – Part 2: Slump test, 2009.
[24] EN 12390, Testing hardened concrete – Part 3: Compressive strength of test specimens, 2009.
[25] Jorg Schlaich, Kurt Schäfer, Mattias Jennewein, Toward a consistent design of structural concrete, PCI J. 32 (3) (1987) 74–150.
[26] Michael Schlaich, Georg Anagnostou, Stress fields for nodes of strut-and-tie models, J. Struct. Eng. 116 (1) (1990) 13–23.
[27] EN 1992-1-1. Eurocode 2, Design of concrete structures - Part 1-1: General rules and rules for buildings, 2004.
[28] Computer & Structures Inc, CSI Analysis Reference Manual, 2011.